J Therm Spray Tech
https://doi.org/10.1007/s11666-025-02148-4

ORIGINAL RESEARCH ARTICLE

New Interface for PEM Electrolysis by Thermally Sprayed BPP-PTL Coating System

K. Bobzin[1] · H. Heinemann[1] · M. Erck[1] · K. Radermacher[1]

Submitted: 1 July 2025 / in revised form: 9 December 2025 / Accepted: 11 December 2025

Abstract In order to take climate action for carbon neutrality, green hydrogen should be implemented in all industrial sectors. The proton exchange membrane water electrolyzer (PEMWE) allows sustainable hydrogen production if electrolyzer lifetime can be balanced with the production costs. In terms of electrolyzer effectiveness, ohmic losses from interfacial contact resistances between the cell components have to be reduced. In this study, a new two-step approach in interface modification of cell components is discussed. Firstly, a steel-based bipolar plate (BPP) is coated by cold gas spraying. Secondly, a cold gas-sprayed porous transport layer (PTL) is directly applied onto the coating, reducing construction gaps in the cell design. The interface modification is evaluated by measuring the total resistance of the BPP-PTL coating system. Accordingly, the electrical resistance between BPP and PTL is successfully reduced by approximately 40% through this approach. The reason for this observation is that BPP and PTL are joined in a new way, namely by mechanical interlocking. The newly developed BPP-PTL coating system is a promising approach for interface modification in the context of PEMWE.

Keywords green hydrogen · cold gas spraying · titanium

Introduction

To achieve significant CO_2 reductions, transitioning to hydrogen-based technologies is essential. In Europe, large-scale hydrogen production today is based on fossil fuel-powered processes. One example for this production process is steam reforming, which produces approximately 9 tons of CO_2 for 1 ton of hydrogen (Ref 1). Producing carbon-free 'green' hydrogen is possible with water electrolysis powered from renewable energy. Among various electrolysis technologies under industrial development, proton exchange membrane water electrolysis (PEMWE) is of special interest, sharing similarities with the well-established proton exchange membrane (PEM) fuel cell. A schematic representation of the PEMWE system is provided in Fig. 1.

The PEMWE cell consists of two half cells of anode and cathode. On the anode, water is fed into the cell on one bipolar plate (BPP) side, transported through a porous transport layer (PTL) and oxidized into oxygen and protons by the anodic catalyst layer. The oxygen is transported out of the cell through the PTL again, and the protons migrate through the membrane where they are reduced to hydrogen by the cathodic layer. In traditional designs, BPPs function as current collectors and separator plates between the stacked cells. PTLs are used to control mass transport, electrical contact to the anode and manage heat transport.

This article is an invited paper selected from presentations at the 2025 International Thermal Spray Conference, held May 5–8, 2025, in Vancouver, Canada, and has been expanded from the original presentation. The issue was organized by Giovanni Bolelli, University of Modena and Reggio Emilia (Lead Editor); Fardad Azarmi, North Dakota State University; Sara Bagherifard, Politecnico di Milano; Partha Pratim Bandyopadhyay, Indian Institute of Technology, Kharagpur; Šárka Houdková, University of West Bohemia; Heli Koivuluoto, Tampere University; Yuk-Chiu Lau, General Electric Power (Retired); Hua Li, Ningbo Institute of Materials Technology and Engineering, CAS; Sinan Müftü, Northeastern University; and Filofteia-Laura Toma, Fraunhofer Institute for Material and Beam Technology.

✉ K. Radermacher
radermacher@iot.rwth-aachen.de

[1] Surface Engineering Institute (IOT), RWTH Aachen University, Aachen, Germany

Published online: 08 January 2026

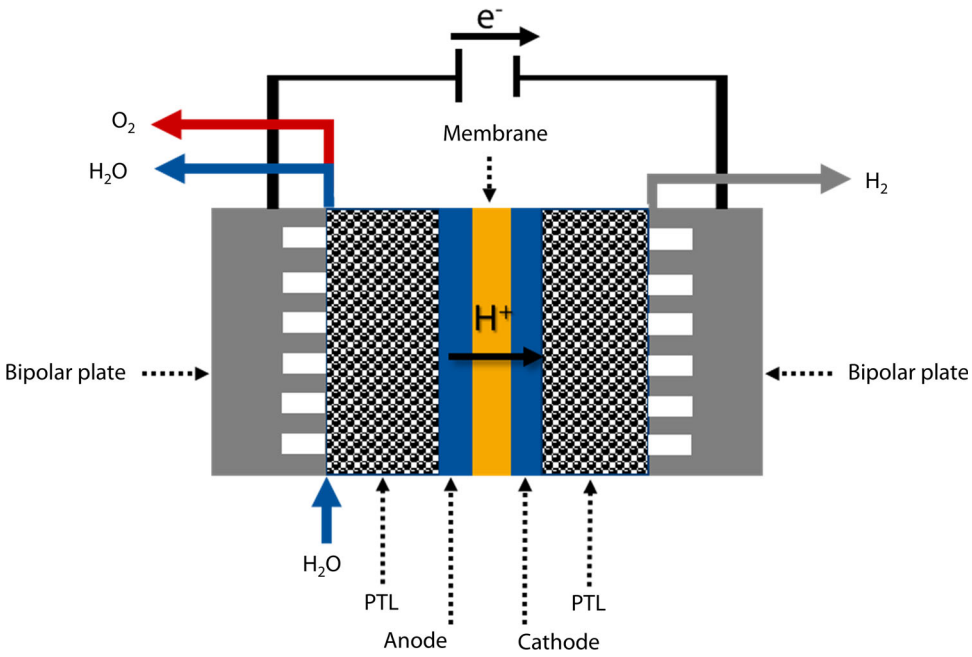

Fig. 1 Schematic illustration of the PEMWE cell (Ref 2), anode: Ir catalyst, cathode: Pt catalyst. Reprinted with the permission of ASM International. All rights reserved

On the anodic side, the cell components of BPP and PTL face special electrochemical conditions in terms of a high electrochemical potential, E = 2 V, and a low pH, pH ≈ 2. Consequently, in order to achieve low electrochemical degradation from corrosion, present BPPs and PTLs are manufactured from titanium, grade 1 to 2. The chosen material exhibits two economic challenges: Firstly, commercially pure titanium is an expensive material compared to stainless steel or nickel-based alloys, commonly used in chemical applications, and secondly, the material bears undesired forming properties necessary for the production of transport channels. For these reasons, alternative material strategies, i.e., coated stainless steel BPPs, are being investigated right now.

For the commercial expansion of PEMWE, future performance targets have been published by U.S. Department of Energy (DoE) (Ref 3), demanding for a development of electrolyzer cells with higher current densities while reducing cell voltage at the same time compared to the status quo. The cell voltage depends on the following equations: (Ref 4)

$$U_{cell} = U_{rev} + U_{\eta\Omega} + U_{\eta A} + U_{\eta K} \quad \text{(Eq 1)}$$

And (adapted from (Ref [5]))

$$U_{\eta\Omega} = (R_{BPP} + R_{PTL} + R_{Membrane}) \cdot i \cdot A \quad \text{(Eq 2)}$$

The reversible voltage U_{rev} describes the minimal voltage required to electrolyze water. It is calculated with the Nernst equation. Under constant gas pressure and temperature, U_{rev} is constant. The Ohmic overpotential $U_{\eta\Omega}$ and the overpotentials at the anode $U_{\eta\mathrm{A}}$ and cathode $U_{\eta\mathrm{K}}$ are remaining variables. The Ohmic overpotential is influenced by the thickness of the polymeric membrane, the specific resistances of the materials and the interfacial contact resistances (ICR) between BPP and PTL and PTL and membrane. Additional resistances have to be considered if the BPP is structured with transport channels (Ref 5). The ICR is a contact resistance depending on the torque applied to assemble the cell components in a stack. Because of the electrochemical conditions, the interface BPP | PTL is subject to alterations through metal dissolution or electrochemical passivation which affect the ICR. Therefore, the interface BPP | PTL is an important developmental factor for the PEMWE.

Thermal Spraying for PEMWE Cell Components

The motivation to test thermal spraying for BPP and PTL stems from the economic desire to reduce manufacturing costs in comparison with thin film technology and also the growing trend of using cold gas spraying in additive manufacturing. Regarding thermal spraying processes in air, cold gas spraying (CGS), high-velocity oxy- and air fuel spraying (HVOF and HVAF) were evaluated for BPP coatings in a previous study by the authors (Ref 6). Titanium CGS coatings showed structurally very promising properties as they exhibit a high coating density and a low degree of oxidation.

As described above, the PTL is an important cell component regarding mass, heat and electron transport. However, the identification of the most effective PTL structure or combination of layers is still part of research. Figure 2 illustrates the two different concepts of a) PTL and b) PTL with micro porous layer (MPL).

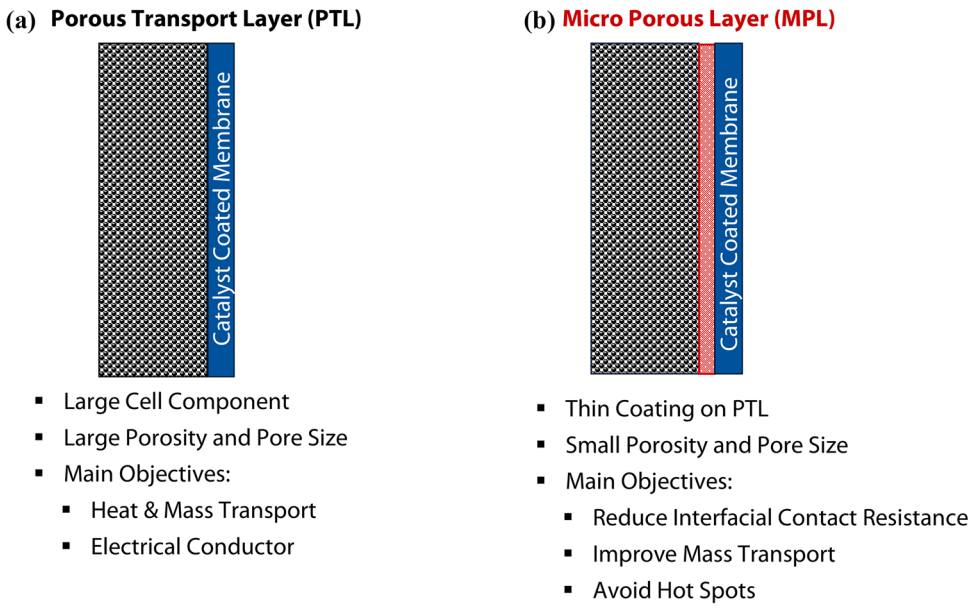

Fig. 2 Schematic Illustration of a) PTL and adjacent catalyst coated membrane b) the addition of a MPL between PTL and catalyst coated membrane

As shown in Fig. 2(a), the PTL is a large cell component in direct contact with the catalyst coated membrane (CCM). Many different types of PTL are currently available on the market from rather thick expanded metal PTLs of 1.5 mm $\leq s \leq$ 3.0 mm to thinner PTLs manufactured from sintered powders or fibers, 0.25 mm $\leq s \leq$ 1.0 mm. In terms of porosity, it was determined by Grigoriev et al. (Ref 7) that it should range between $30\% \leq \Phi \leq 50\%$ for a suitable ratio between mass and electric transport. In the same publication, the authors also pointed out that a graded pore structure is beneficial. A graded structure enhances mass transport and electrical contact with the CCM. For those reasons, a MPL is employed, which can be viewed as a surface modification of a larger PTL, and is depicted in Fig. 2(b) in red. In the context of thermal spraying, there is one publication showing the use of thermal spraying to generatively produce a three-dimensional cell component, and there are several publications employing thermal spraying for MPL deposition. A brief literature review is given in the following sections.

Vacuum Plasma Spraying/Atmospheric Plasma Spraying

Right up from the beginning, German Aerospace Center (DLR) was focusing on generating graded PTL structures with large pores on the BPP side and very fine pores on the CCM side. In Lettenmeier et al. (Ref 8) for example, the aim was to deposit a multilayer system with VPS, differing in pore size, on a commercially available sintered PTL. Therefore, different Ti-powder fractions, F = 125 µm and F = 45 µm, are used. Comparing the surface properties of the VPS coating and the sintered product, a higher roughness for the VPS coating with the coarser powder with 12 µm $< Ra,$ VPS $<$ 17 µm compared to Ra, Sinter $\approx$ 7.7 µm ± 0.3 µm is observed. This is rather undesired as the coating is directly pressed into the soft polymer membrane and might cause a non-homogenous contact or even membrane rupture. Using the finer powder of F = 45 µm, average surface roughness is rather similar to the commercial PTL with Ra, VPS $\approx$ 9 µm ± 1 µm. Regarding the porosity, no large difference between the coatings from finer powder and the combination of finer and coarser layers is identified. The porosity ranges between $20\% < \Phi < 30\%$. Pore sizes were determined with mercury intrusion porometry. The pore radii vary between 3 µm $< Dp <$ 5.5 µm depending on the number of passes and choice of powder.

While the results from that study demonstrate promising coating structures, VPS is cost-intensive and a less scalable thermal spraying process. For those reasons, Surface Engineering Institute (IOT) studied the use of atmospheric plasma spraying, which is reported in (Ref 9). Main conclusions from that investigation are that coating of expanded metals or sintered PTLs with APS is possible, but the surface roughness is high with $Rz >$ 120 µm, the Ti oxidation despite shrouding elevated and the maximum porosity achievable is Φ = 23 %. Consequently, there is a motivation to identify other processes apart from plasma spraying that are suitable to apply porous structures in serial production either as MPL on commercial PTLs or generate fully functional PTLs of larger thickness.

HVOF Spraying

Driven from the motivation to generate a three-dimensional fully functional PTL, the use of HVOF was shown in context of PTL development by IOT (Ref 2). Gas-fueled HVOF was utilized by setting up a hydrogen surplus which led to lower particle velocities and a reductive atmosphere. Because of a special separation technique from the substrate, the resulting PTL exhibits a porosity gradient with three zones as reported in (Ref 10). On the impact side, the separated surface is very smooth, Ra = 1 µm, making this side suitable for membrane contact. The average roughness of the build-up side is Ra = 14 µm which is directed to the BPP. The high surface roughness reflects the higher porosity on the surface in the BPP contact, promoting mass transport, which decreases after 100 µm in the bulk material to an average value of Φ = 32% determined from computer tomography. In the impact region, the porosity further decreases to Φ = 21%. Median pore size is Dp = 4 µm. The functionality of this HVOF-PTL was demonstrated in a single cell test. After the test, the membrane was studied, and imprints of the reference PTL material are more visible in the membrane than of the HVOF-PTL proving that the smooth surface contributes to an improved membrane contact.

Cold Gas Spraying

Next to VPS, CGS is an established technology to process titanium materials. Sievert et al. (Ref 11) used CGS to apply a MPL on an expanded metal. The coating structure can be described as a single layer of spherical Ti particles which was achieved through a high transverse gun speed v_{robo} = 2,000 mm/s and a standoff distance with d_w = 100 mm. Surface roughness was not published, but the functionality was tested in a cell test.

In (Ref 12), a batch of Ti and Cu was processed by CGS. Cu is a pore-forming agent (PFA) in this case that is chemically leached out. Thus, pores remain in the Ti matrix. However, because of high coating density, Cu is entrapped and cannot be leached out properly. Consequently, the porosity measured of this PTL is $\Phi \approx 8\%$ only.

While the PFA approach was not successful, studies in the biomedical field have already demonstrated that CGS can be utilized for the manufacture of larger porous structures without additional powder feedstock modifications. In Wathanyu et al. (Ref 13), multilayer coating systems from titanium for implant applications were investigated. A parameter study was conducted to form pores in the process. Surface roughness of the showed coating structures is Ra = 14 µm, and porosity determined from image analysis is high with $\Phi > 30$ %. The possibility of achieving high porosity with CGS and also the experience from serial production with this process make CGS interesting for further investigation in the context of PEMWE.

Aim of Work

Literature shows that the manufacture of porous Ti structures with cold gas spraying is possible, and regarding the PEMWE application, promising approaches can be identified. While efforts have been made to improve the contact between PTL and catalyst layer on the membrane through the design of MPLs, the interface BPP | PTL has not been considered so far. The aim of this work is to demonstrate improved electrical contact between BPP and PTL through a BPP-PTL coating system manufactured from direct application of the PTL on top of the BPP with CGS. In contrast to (Ref 12), PFA is not used to achieve the porous structure in this study, but process parameters are being modified. The working hypothesis is that direct application leads to mechanical interlocking of both components. The BPP-PTL coating system is intended to contribute to a future zero-gap cell design which leads to reduced ohmic losses and results in an increased cell performance.

Experimental

Process Development for CGS-PTL

Both, BPP coating and PTL, were deposited with the CGS system Evo CSII 6/11, Impact Innovations GmbH, Rattenkirchen, Germany, on 316L-substrates of d = 0.5 mm thickness. Because of the comparably thin part thickness, substrate preparation was conducted by grinding with P80 sandpaper and cleaning with ethanol. The chosen powder feedstock was an angular HDH titanium grade 4, $F = -45 + 11$ µm, Metco 4010 C, Oerlikon Metco AG, Pfäffikon, Switzerland, and was injected with a powder feeding rate of $\dot{m}$= 0.84 kg/h. In order to produce a highly porous structure, the process parameters between BPP coating and the PTL differ strongly in gas temperature, gas pressure and standoff distance, as given in Table 1. The process development for the PTL was based on PTL-1, − 2, and − 3 using the same process parameters as in (Ref 13). The concept of PTL-3 is to create a two-layer system with a pore gradient. In contrast to the original publication, the pore gradient is designed to increase from surface to substrate while for implant application, a rough and porous surface is desired to favor tissue adhesion. Thus, the new challenge for this parameter of PTL-3 was to avoid densification from the last two passes with p = 30 bar.

Table 1 Overview over process parameters for CGS system Evo CSII 6/11

	Gas Pressure p in bar	Gas Temperature T in °C	Standoff Distance d_w in mm	Passes	Meander Width b in mm	Robot Speed v in mm/s
BPP-coating	48	1,100	30	1	1	500
PTL-1	20	550	30	10	2	500
PTL-2	30	550	30	10	2	500
PTL-3	20, 30	550	30	8, 2	2	500
PTL-4	20	550	60	3	1	500
PTL-5	20	550	90	3	1	500
PTL-6	20	550	120	3	1	500
PTL-7	20	550	150	3	1	500
PTL-8	20	550	180	3	1	500
PTL-9	20	550	200	3	1	500

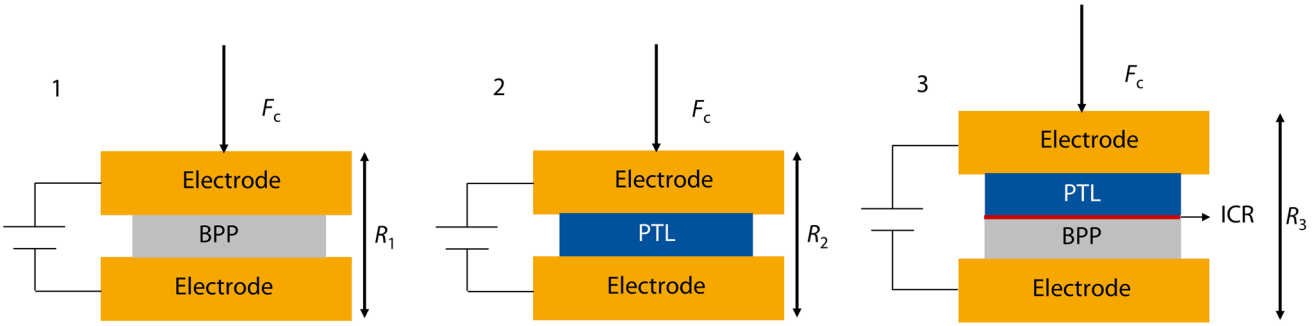

Fig. 3 Schematic illustration of three-step ICR measurement, Step 1: Measurement of BPP resistance R1, Step 2: Measurement of PTL resistance R2, Step 3: Resistivity measurement of combined BPP and PTL

Pressure elevation was conducted when the gun was pausing in home position.

The cross-sections of PTL-1, − 2 and-3 in the result section, in Fig. 5, show that the coating structures of the porous layers do not meet the expectations. Consequently, process development was necessary. The authors decided that the selected gas temperature and pressure were suitable enough to process the titanium powder at hand. Thus, the standoff distance was systematically increased (PTL-4 to − 7) aiming at reducing the kinetic energy at the particle impact and causing a porous structure.

Measurement of Interfacial Contact Resistance

The methodological approach for the experimental measurement of the ICR is based on Lædre et al. (Ref 14). The ICR is calculated from a three-step measurement, as illustrated in Fig. 3.

The general setup consists of two gold-plated copper electrodes which are pressed together under various loads. The sample is placed between the electrodes and a current is applied. The voltage drop is measured, and the total resistance is calculated with the ohmic law. According to Lettenmeier et al. (Ref 15), the range of 120 N cm^{-2} $\leq F_c \leq$ 200 N cm^{-2} in compaction force is technically relevant for clamping all stack components together. Through the applied compaction force, gaps and voids are eliminated leading to a maximization of contact area and consequently to a decrease in the ICR.

First, the resistance $R1$ is measured with the BPP. $R1$ consists of the intrinsic resistances of the copper electrodes R_E and of the BPP R_{BPP} as well as the two contact resistances at the interface between the electrodes and the BPP $R_{E/BPP}$. The definition of $R1$ is shown in equation 3.

$$R_1 = 2 \cdot R_E + R_{BPP} + 2 \cdot R_{E/BPP} \quad \text{(Eq 3)}$$

Second, resistance $R2$ is measured with PTL in the same way as resistance $R1$ is measured. Resistance $R2$ is defined according to Eq. 4.

$$R_2 = 2 \cdot R_E + R_{PTL} + 2 \cdot R_{E/PTL} \quad \text{(Eq 4)}$$

In the last step, resistance $R3$ with BPP and PTL is determined. Equation 5 shows the resistance $R3$.

$$R_3 = 2 \cdot R_E + R_{PTL} + R_{BPP} + R_{E/PTL} + R_{E/BPP} + R_{BPP/PTL} \quad \text{(Eq 5)}$$

Due to the high electrical conductivity of the copper electrodes and the associated low ohmic resistance, the intrinsic resistance of the copper electrodes R_E is neglected (Ref 16). As the single resistance of the BPP RBPP is significantly lower than the contact resistance at interfaces, it is negligible for the calculation of the ICR (Ref 17). The same has been observed for R_{PTL} by the authors in a preliminary study. The subtraction of the two contact resistances $R_{E/PTL}$ and $R_{E/BPP}$ leads to the determination of the contact resistance $R_{BPP/PTL}$. This is shown in eq. 6.

$$R_{BPP/PTL} = R_3 - \frac{1}{2} \cdot (R_1 + R_2) \quad \text{(Eq 6)}$$

By multiplying $R_{BPP/PTL}$ with area A, the ICR can be determined, cf. eq. 7.

$$ICR = R_{BPP/PTL} \cdot A \quad \text{(Eq 7)}$$

The ICR-measurement stand was specially designed and built-up in the framework of the research project. To this day, there is no standardization of the ICR measurement. The determination of low ohmic resistances, such as the ICR, is based on the principle of four-wire measurement. A constant electrical current of $I = 1.00 \pm 0.01$ A is applied to the gold-plated copper electrodes via an external direct current source AL781NX, elc, France, using Kelvin clamps. The resulting voltage drop between the electrodes is measured using a dual-display multimeter, Fluke, Everett, Washington, USA, after a holding time of $t = 15 \pm 1$ s at a constant force. The measurements are conducted in a range of compaction force of 40 N cm^{-2} $\leq F_c \leq$ 200 N cm^{-2}.

The ICR according to Eq. 5 is determined on three variations:

- Variation 1**:** Steel BPP (316L, $s = 0.5$ mm) | Ti-Fiber-PTL (Titanium Grade 1, $s = 0.25$ mm, NV Bekaert SA, Belgium)
- Variation 2: Titanium BPP (Grade 1, $s = 0.1$ mm) | Ti-Fiber-PTL
- Variation 3: Ti-coated Steel BPP (cf. Table 1) | Ti-Fiber-PTL

In order to mimic real PEMWE interfaces, the chosen PTL in this publication is a Ti-Fiber-PTL and not a carbon-based gas diffusion layer. The morphology of the PTL from Bekaert SA is analyzed thoroughly by Stiber et al. in (Ref 18). The newly developed CGS-PTL is compared to the structure of the commercial Ti-Fiber-PTL. For the directly applied PTL on the coated BPP (Variation 4), the ICR cannot be determined because a detached CGS-PTL could not be manufactured without damaging the PTL or the BPP coating. Yet, the total resistance $R3$ is compared between the BPP-PTL pairings named above and the directly applied CGS-PTL.

Scanning Electron Microscopy (SEM)

Metallographic cross-sections were prepared according to DVS Merkblatt 2310-1. SEM Phenom XL G2, Thermo Fisher Scientific, Netherlands, is utilized with an acceleration voltage of $U_B = 15$ kV and backscattered electron detector. The sample chamber is evacuated to a pressure of $p = 10^{-6}$ bar. Coating thickness is averaged through the largest distance and the smallest distance between substrate and surface each cross-section. For porosity analysis, nine images are extracted at a magnification of $V = 1{,}500$x.

Confocal Laser Scanning Microscopy (CLSM)

In a previous study by the authors (Ref 10), the CCM was investigated in SEM after the single cell test. Accordingly, heavy marks from the Ti-Fiber-PTL can be observed in the CCM, while for the CCM contacted with the smooth side of the HVOF-PTL, this effect is less pronounced. Consequently, PTL roughness has a large influence on the contact to the thin and polymeric membrane. Thus, CLSM VK X-210, Keyence Instruments Ltd., Japan, is used with 20x-magnification and a step size of $h = 0.50$ µm to analyze the roughness. Roughness analysis is conducted with the VK X-Analysis Module by Keyence according to ISO 4287:1997. For roughness analysis of the coatings, a profile average of six lines is extracted and length of $ln = 12.5$ mm is analyzed with the filters $\lambda c = 2.5$ µm, $\lambda s = 1.055$ µm. The roughness test is conducted on nine samples for the PTLs and 18 samples for the BPP coating.

Carrier Gas Hot Extraction

Carrier gas hot extraction is applied to determine the oxygen level in the PTL. Small fragments are obtained by coating a tape in the same process as the metallic components. Three fragments are tested with G8 Galileo ON/H, Bruker AXS, Germany, at RWTH Welding and Joining Institute.

Results

Measurement of BPP-ICR

The BPP coating is applied according to Table 1 with CGS on a $s = 0.5$ mm thin 316L steel sheet. This coating is compared with uncoated materials regarding the ICR between the BPP and the Ti-Fiber-PTL. Therefore, the ICR

is measured by testing five BPP and PTL segments in a size of Asample = 25 mm × 25 mm of each variation for five times. The average ICR for each variation is calculated out of those 25 measurements. In Fig. 4, the average ICR dependency on the compaction force is depicted.

As explained, the ICR decreases with increasing compaction force. In the relevant force range, uncoated titanium and 316L exhibit similar behavior while the coated BPP shows lower ICR values. One hypothesis is that the roughness peaks in the as-sprayed state penetrate the pores between the fibers, and thus the number of electron pathways rises and the electron transfer is improved. However, blocking the pores with the roughness peaks could inhibit mass transport. This challenge could potentially be solved by directly applying the PTL onto the coated BPP, which is discussed in the following chapter.

Development of CGS-PTL

The process development for the porous CGS structure focuses on gas pressure variation and modification of standoff distance. In Fig. 5, the structures for PTL-1 to − 3 are compared which were generated through gas pressure variation using SEM images. PTL-1, shown in Fig. 5(a), was produced with ten passes at p = 20 bar gas pressure. Image analysis provides coating thickness including the thickness deviation from roughness. For PTL-1, the thickness ranges between 900 µm < s < 1,000 µm with the roughness peaks. This coating thickness is in good agreement with the original reference (Ref 13) in which a coating thickness of $s \approx$ 100 µm for one pass is reported. However, coating porosity of the obtained coating is approximately half as high as described in the original reference. A reason for this might be that the chosen Ti powder has a fraction of finer particles, d_{10} = 11 µm, that is not included in the powder from the reference with F = − 44 + 20 µm. The fine particles are better plasticized in the hot gas stream and lead to less pore formation. Therefore, the porosity is lower than in the original reference.

Regarding PTL-2, in Fig. 5(b), porosity and coating thickness are decreased when increasing the process gas pressure from p = 20 bar to p = 30 bar. The reason for this observation is the higher kinetic impact of the Ti particles on the substrate through the higher gas pressure leading to a strong densification effect. In a third option, eight passes with the lower gas pressure and two passes with the higher gas pressure are combined with the intention to obtain a pore gradient from high porosity at the interface to lower porosity in the surface region. Figure 5(c) demonstrates that the chosen approach is not successful. Firstly, there is no strong difference in pore structure between the eight passes and the final two passes. Secondly, the expected coating thickness for PTL-3 is $s \approx$ 950 µm, but the real coating thickness of PTL-3 is s = 720 µm ± 30 µm and therefore lower than expected. The authors assume that the higher gas pressure leads to coating erosion of already deposited layers.

Continuing with the variation of standoff distance, Fig. 6 shows SEM images of five different pore structures. Accordingly, increasing the standoff distance results in an increase in porosity. However, the pore structures achieved with a range of 60 mm ≤ d_w ≤ 120 mm in standoff distance are presumably still too dense to function as gas- and water-permeable PTL. Increasing the standoff distance to d_w ≥ 180 mm, the pore diameters visually increase and the powder particle shape becomes more pronounced. This indicates a lower particle plasticization and a lower kinetic energy at the particle impact on the substrate than for the other standoff distances. While the pore size and particle shape seem favorable, in this range of standoff distance, the coating deposition becomes more inhomogeneous. At d_w = 200 mm, less particles adhere because of the weakened particle impact. Consequently, the coating thickness and coating cohesion is reduced. To sum up, for d_w = 180 mm and d_w = 200 mm, the loss in coating quality is greater than the technical benefit gained from the high porosity.

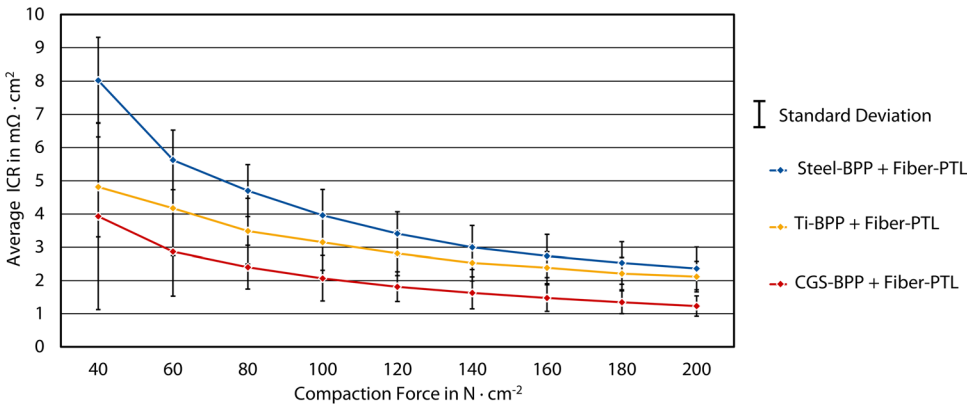

Fig. 4 Calculated ICR, averaged from five measurements, in the compaction force range from 40 N/cm^2 to 200 N/cm^2 for unstructured steel BPP, Ti-BPP and steel BPP coated with Ti by CGS. In the measurement, the PTL is a commercial uncoated Ti-Fiber-PTL

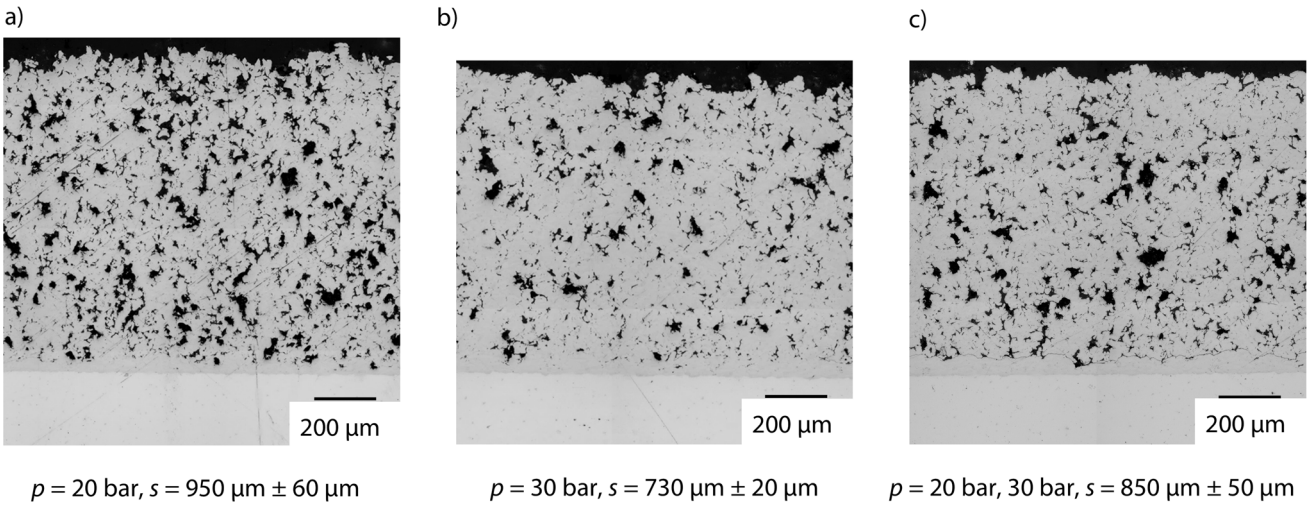

Fig. 5 Comparison of (a) PTL-1 from 10 passes at 20 bar, (b) PTL-2 from 10 passes at 30 bar and (c) PTL-3 from 8 passes at 20 bar and 2 passes at 30 bar

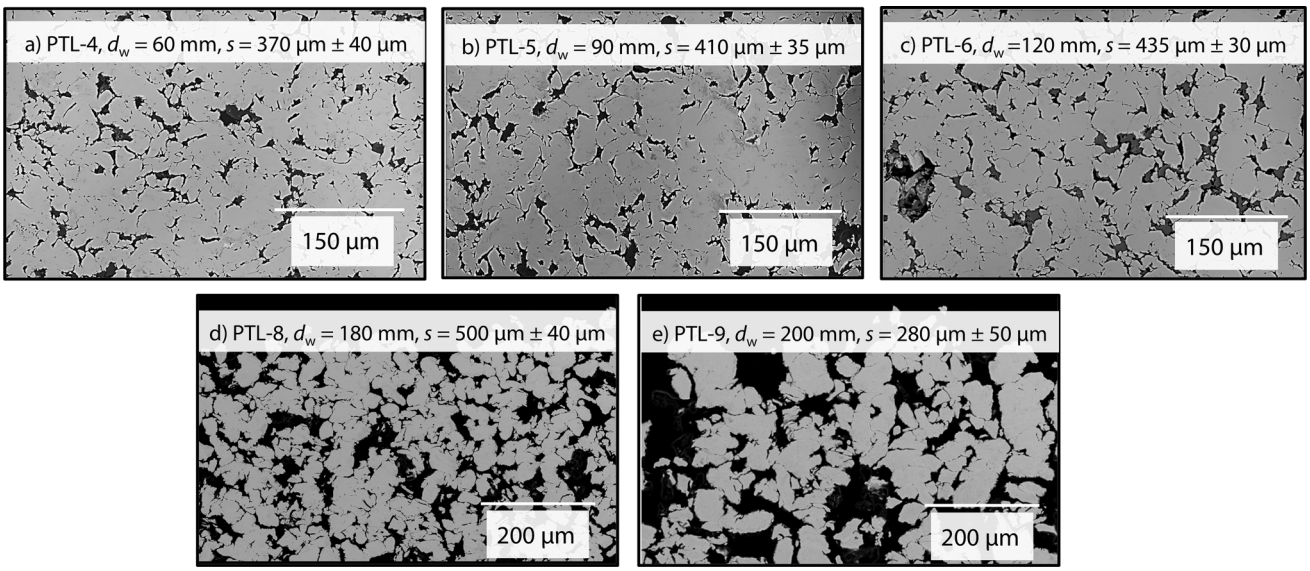

Fig. 6 (a) to (e): Comparison of PTL-4 obtained with a standoff distance of d_w = 60 mm, PTL-5 with a standoff distance of d_w = 90 mm, PTL-6 with a standoff distance of d_w = 120 mm, PTL-8 with a standoff distance of d_w = 180 mm and PTL-9 with a standoff distance of d_w = 200 mm

With the standoff distance of d_w = 150 mm, the microstructural criteria are met. For this reason, this standoff distance is employed to directly apply the PTL-7 on the CGS-coated steel sheet. In order to illustrate the generated coating structure, Fig. 7 shows three exemplary cross-sections of the BPP-PTL coating system.

According to an image analysis with ImageJ (Ref 19), the pores are connected in a pore network in PTL-7. On the BPP interface region, larger pores than in the surface region can be identified which are necessary in order to transport water from the BPP to the catalyst layer. Determining Feret's diameter, 50% of the pore network is constituted out of pores, narrowings and fine channels in a range of $0.1 \leq Dp \leq 1$ µm. Because of the chosen angular powder feedstock, the pore structure of all sprayed PTLs is angular as well. The largest diameter encompasses approx. $Dp \approx 100$ µm. Moreover, overall porosity is estimated to be $\Phi \approx 24 \pm 2\%$.

Surface properties of the produced PTL are compared to the commercial Ti-Fiber-PTL and the BPP coating shown in Fig. 8. The boxplots depict the arithmetic average, the median, and the interquartile range in between the first and third quartile as well as the upper and lower outliers.

The analysis of Ra in Fig. 8(a) shows that the commercial product is on average rougher, but the variance is larger for the CGS-PTL. Out of the nine measurements, there is just one found with a Ra value of $Ra \approx 6$ µm. However, this outlier is not significant according to Dixon

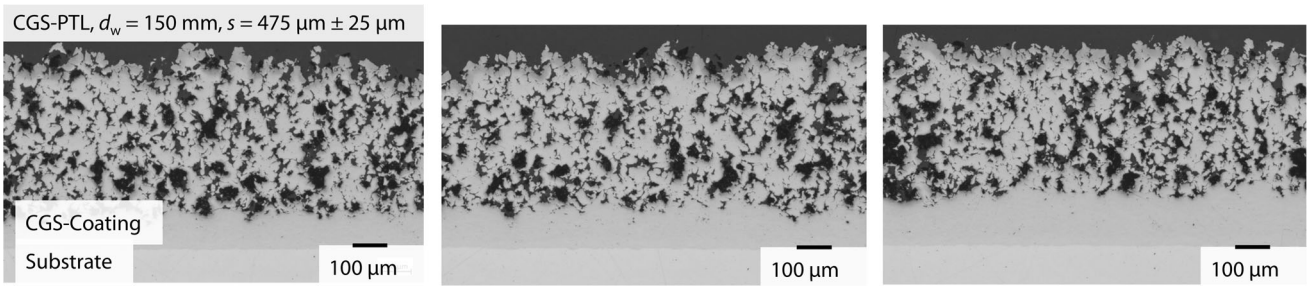

Fig. 7 Three exemplary cross-sections of PTL-7, obtained with a standoff distance of d_w = 150 mm, which is identified as a suitable standoff distance for the application

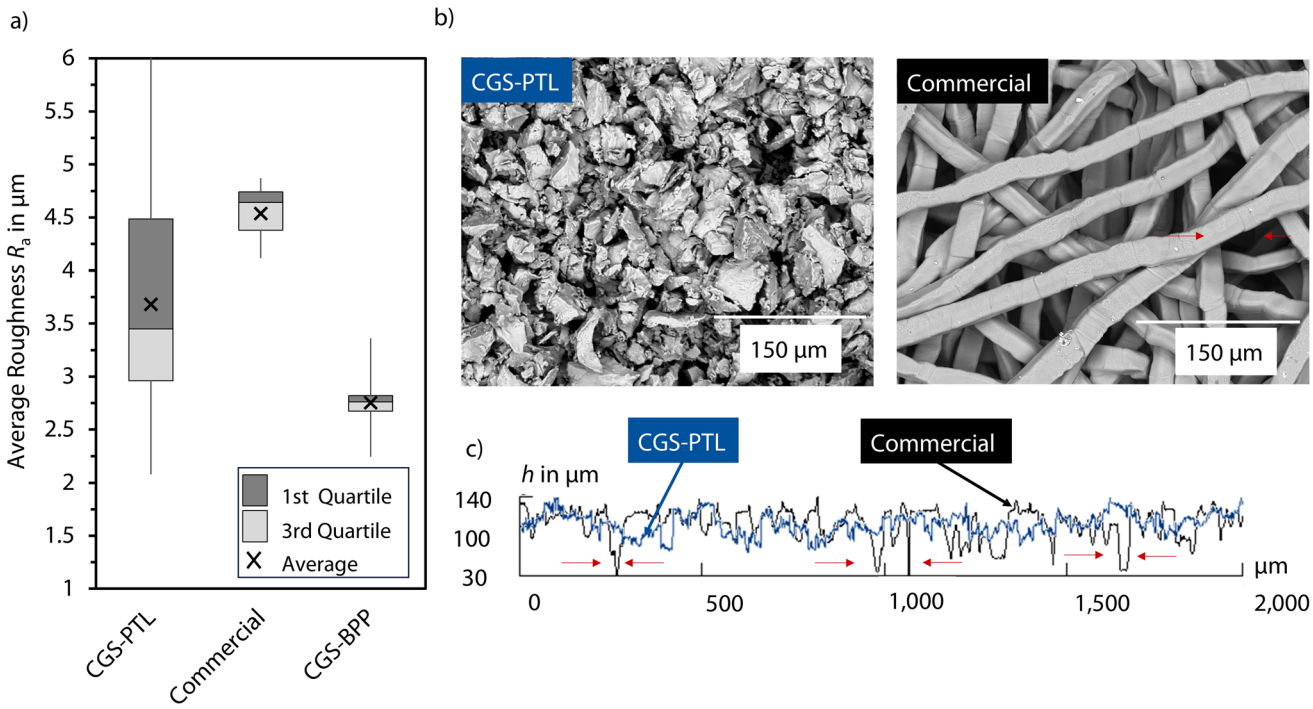

Fig. 8 (a) Average roughness *R*a in µm for the PTL-7, the commercial Ti-Fiber-PTL and the CGS-BPP coating, (b) REM image of the surface of PTL-7 and commercial Ti-Fiber-PTL and (c) exemplary height profiles determined for PTL-7 and commercial Ti-Fiber-PTL

test so it cannot be excluded from the analysis. Figure 8(b) depicts the surface of the two different PTLs from a top view in the SEM and Fig. 8(c) shows an exemplary height profile recorded from the CLSM. Accordingly, the surface profile of the commercial sintered Ti-Fiber product is characterized by substantial height differences of more than Δh = 100 µm between the fiber surface and the depth of the pores representing a pore-rich surface of deep pores. The profile of the CGS-PTL indicates that the surface is less perforated with deep pores and the SEM image underlines that the coating surface is constituted out of smaller pores. Carrier gas hot extraction reveals that the CGS-PTL exhibits an oxygen level of ω(O2) = 0.32 ± 0.09 mass-% which is in the range of the oxygen level determined with the same method for the commercial Ti-Fiber-PTL of ω(O2) = 0.30 ± 0.02 mass-%. Furthermore, the oxygen level is lower than the generatively manufactured HVOF-PTL, ω(O2) = 1.12 mass-%, published by the authors in (Ref 10) underlining the advantages of CGS over other thermal spraying processes in atmosphere.

Comparison of *R*3

The equations in the experimental section describe that the ICR is determined in a three-step measurement. Since the directly applied CGS coating could not be produced in a free-standing manner, the ICR is not considered to quantify the newly developed BPP-PTL interface but *R*3 according to eq. 5 is compared between all variations. Table 2 Illustrates the results at F_c = 140 N cm^{-2}.

As shown in Table 2, the single resistance of the PTL adds the largest contribution to the total resistance *R*3.

Table 2 Overview of the resistance R3 measured at $Fc = 140$ N cm^{-2}

	$R1$ in mΩ	$R2$ in mΩ	$R3$ in mΩ
Steel BPP | Ti-Fiber-PTL	0.32 ± 0.02	0.78 ± 0.05	1.05 ± 0.19
Ti-BPP | Ti-Fiber-PTL	0.45 ± 0.01	0.80 ± 0.05	0.93 ± 0.09
CGS-coated BPP | Ti-Fiber-PTL	0.47 ± 0.09	0.93 ± 0.16	0.89 ± 0.09
CGS-BPP-PTL Coating System	…	…	0.57 ± 0.1

Looking at the cold gas-sprayed BPP-PTL coating system, the smallest $R3$ is exhibited. In this case, the reduction is almost 40% in comparison with the combination of CGS-coated steel BPP and a commercial Ti-Fiber-PTL.

Discussion

As shown in Fig. 7, CGS-PTL and CGS-coated BPP form a zero-gap joint. The roughness of the cold gas-sprayed BPP coating is beneficial for the joining of BPP and PTL since it promotes mechanical interlocking between the coating and the CGS-PTL. Even though titanium is processed in air with the CGS process, the oxygen content of the produced PTL is comparable to the commercial fiber product. The results from Table 2 indicate that the zero-gap design from direct application of the PTL on the BPP reduces contact resistance.

Regarding the porosity, on the one hand, the developed CGS-PTL shows an overall porosity slightly lower than the recommended porosity of $\Phi = 30\%$ from Grigoriev et al. (Ref [7]) which could impede the two-phase transport. Yet, it was assumed that the pore size increases from the BPP interface to the surface, since the gradual coating built-up from particle impact takes place with a high amount of kinetic energy, typically leading to a densification effect. In contrast, the developed CGS-PTL exhibits large pores at the BPP interface and smaller pores in the surface region which will be positioned toward the electrode in the PEMWE single cell. As described in the literature review, this pore gradient is very much in favor of the application and is achieved without any additional agent or modification of powder feedstock. The in situ formation of larger pores at the BPP interface is promising as large pores are needed for the phase transport initiation on the BPP side. Furthermore, the pores in the CGS-PTL are interconnected potentially allowing in-plane transport on the BPP side and bidirectional through-plane transport to the electrode.

Regarding the surface properties of the CGS-PTL, the average roughness is lower than the VPS (Ref 8), APS (Ref 9) and of the build-up side of the HVOF-PTL (Ref 10). Furthermore, the average roughness of the commercial PTL is higher as well. The variance of Ra values can probably be attributed to the differences in coating thickness within an average of 40 µm. This could be controlled by post-processing the PTL, e.g., by grinding. As the PTL surface is in direct contact with the electrode, the CGS-PTL shows favorable properties due to a finer pore and particle structure and a lower roughness.

Conclusions

CGS is used to coat a $s = 0.5$ mm thin 316L-sheet with titanium and to create a coating system by adding a PTL. In this way, a special economic advantage is demonstrated since the same coating process for BPP coating and PTL is utilized. By directly applying the PTL on the BPP, a zero-gap design in a PEMWE cell can be realized, and a new interface toward the electrode is generated. In order to quantify the new design improvement, the measurement of contact resistance was conducted with a lab-designed test stand for smaller sample segments. The results of the measurement showed that this zero-gap design can lead to a reduction in electrical resistance by approximately 40%.

Outlook

In order to evaluate electrochemical performance, corrosion tests and cell tests should be conducted. The fine pore structure and lower roughness on the PTL surface open opportunities to use this type of PTL as MPL. Using a PTL as substrate material leads to a different impact behavior of the powder particles, and also the different mechanical properties of the substrate must be considered. For this reason, coating development on PTL substrates is necessary.

Acknowledgements The H2Giga-project StacIE (03HY103B) is funded in the context of the competition of ideas 'Wasserstoffrepublik Deutschland' by German Federal Ministry Research, Technology and Space and by the European Union.

Funding Open Access funding enabled and organized by Projekt DEAL.

References

1. M. Muron, "Clean Hydrogen Monitor 2022", Bruxelles, 2022.
2. K. Bobzin, L. Zhao, H. Heinemann, and E. Olesch, Highly Porous Titanium Coatings For Proton Exchange Membrane Water Electrolysis Application By HVOF, ITSC 2024 International Thermal Spray Conference and Exposition, DVS Media, Ed., May 2024 (Milan), 2024, p. 291–297.
3. U.S. Department of Energy, Doe Technical Targets For Polymer Electrolyte Membrane Fuel Cell Components, 2025. https://www.energy.gov/eere/fuelcells/doe-technical-targets-polymer-electrolyte-membrane-fuel-cell-components. Accessed April 16, 2025.
4. H. Wendt and G. Imarisio, Nine Years of Research and Development on Advanced Water Electrolysis. A Review of the Research Programme of the Commission of the European Communities, *J. Appl. Electrochem.*, 1988, **18**(1), p 1–14.
5. B. Han, S.M. Steen, J. Mo, and F.-Y. Zhang, Electrochemical Performance Modeling of a Proton Exchange Membrane Electrolyzer Cell for Hydrogen Energy, *Int. J. Hydrogen Energy*, 2015, **40**(22), p 7006–7016.
6. K. Bobzin, H. Heinemann, E. Olesch, and K. Radermacher, Development of Dense and Low Oxide Titanium Coatings For PEMWE Application, ITSC 2024 International Thermal Spray Conference and Exposition, DVS Media, Ed., May 2024 (Milan), 2024, p. 1–7.
7. S.A. Grigoriev, P. Millet, S.A. Volobuev, and V.N. Fateev, Optimization of Porous Current Collectors for Pem Water Electrolysers, *Int. J. Hydrogen Energy*, 2009, **34**(11), p 4968–4973.
8. P. Lettenmeier, S. Kolb, N. Sata, A. Fallisch, L. Zielke, S. Thiele, A.S. Gago, and K.A. Friedrich, Comprehensive Investigation of Novel Pore-Graded Gas Diffusion Layers for High-Performance and Cost-Effective Proton Exchange Membrane Electrolyzers, *Energy Environ. Sci.*, 2017, **10**(12), p 2521–2533.
9. K. Bobzin, L. Zhao, H. Heinemann, E. Burbaum, and K. Radermacher, Schichtentwicklung für die potenzielle Anwendung in PEM-Wasserelektrolyse, *Therm. Spray Bull.*, 2023, **16**(1), p 42–48.
10. K. Bobzin, S. Finger, L. Zhao, H. Heinemann, E. Olesch, K. Radermacher, S. Pechmann, D. Possart, S.H. Christiansen, D. Hoffmeister, B. Fritsch, S. Thiele, and A. Hutzler, Porosity-Zoned Porous-Transport Layer for Proton-Exchange Membrane Water Electrolysis by High-Velocity Flame Spraying, *Adv. Eng. Mater.*, 2025 https://doi.org/10.1002/adem.202402462
11. T. Sievert, S. Zerressen, M. Bram, A. Glüsen, K. Bender, O. Guillon, and R. Vaßen, Cold Gas Spraying of Titanium on Stainless Steel to Enhance Corrosion Protection Inside Proton Exchange Membrane Water Electrolyzers, *Surf. Coat. Technol.*, 2025, **513**, 132486.
12. M. Fakourihassanabadi, B. Guerreiro, J. Gaudet, M.H. Martin, S. Abbasi, S. Thorpe, and D. Guay, Fabrication of a Ti-based 3D Porous Transport Layer for PEMWE using Shockwave-Induced Spraying and Cold Spray, *Surf. Coat. Technol.*, 2024, **477**, 130353.
13. K. Wathanyu, K. Tuchinda, S. Daopiset, S. Sirivisoot, J. Kondas, and C. Bauer, Study of the Properties of Titanium Porous Coating with Different Porosity Gradients on 316L Stainless Steel by a Cold Spray Process, *J. Therm. Spray Technol.*, 2022, **31**(3), p 545–558.
14. S. Lædre, O.E. Kongstein, A. Oedegaard, F. Seland, and H. Karoliussen, Measuring in situ Interfacial Contact Resistance in a Proton Exchange Membrane Fuel Cell, *J. Electrochem. Soc.*, 2019, **166**(13), p F853–F859.
15. P. Lettenmeier, R. Wang, R. Abouatallah, B. Saruhan, O. Freitag, P. Gazdzicki, T. Morawietz, R. Hiesgen, A.S. Gago, and K.A. Friedrich, Low-Cost and Durable Bipolar Plates for Proton Exchange Membrane Electrolyzers, *Sci. Rep.*, 2017, **7**, p 44035.
16. S. Lædre, C.M. Craciunescu, T. Khoza, N. Vaszilcsin, A. Kellenberger, V. Bolocan, I. Mitelea, and A. Ercuta, Issues Regarding Bipolar Plate-Gas Diffusion Layer Interfacial Contact Resistance Determination, *J. Power. Sources*, 2022, **530**, 231275.
17. H. Tawfik, Y. Hung, and D. Mahajan, Eds., Polymer Electrolyte Fuel Cell Degradation, *Academic Press*, 2011.
18. S. Stiber, N. Sata, T. Morawietz, S.A. Ansar, T. Jahnke, J.K. Lee, A. Bazylak, A. Fallisch, A.S. Gago, and K.A. Friedrich, A High-Performance, Durable and Low-Cost Proton Exchange Membrane Electrolyser with Stainless Steel Components, *Energy Environ. Sci.*, 2022, **15**(1), p 109–122.
19. J. Schindelin, I. Arganda-Carreras, E. Frise, V. Kaynig, M. Longair, T. Pietzsch, S. Preibisch, C. Rueden, S. Saalfeld, B. Schmid, J.-Y. Tinevez, D.J. White, V. Hartenstein, K. Eliceiri, P. Tomancak, and A. Cardona, Fiji: An Open-Source Platform for Biological-Image Analysis, *Nat. Methods*, 2012, **9**(7), p 676–682.